ADVANCED FUNCTIONAL MATERIALS
www.afm-journal.de

Understanding the Chemical and Electronic Properties of Sub-Monolayer TiO_2 on High Surface Area Silica for Jet Fuel Synthesis Applications

Mark A. Isaacs, Charalampos Drivas, Arthur Graf, Sasha Kroon, Santosh Kumar, Junxi Liu, Antonio Torres-Lopez, Cameron Price, Edward Garland, Ines Lezcano-Gonzalez, Christopher. M. A. Parlett, Vannia C. dos Santos-Durndell, and Lee J. Durndell**

2.5% of global carbon emissions result from air travel, underscoring the need for sustainable aviation fuels (SAF) derived from second-generation lignocellulosic biomass to enhance the green credentials of the aviation sector. This study demonstrates the first solvent-free photocatalytic conversion of furfural (FAL) and cyclopentanone (CPO) to produce 2,5-bis(2-furylmethylidene)cyclopentanone (F_2Cp), a jet fuel precursor, using Ti-SBA-15 catalysts, synthesized via alkoxide grafting and controlled titanium surface coverage. Sub-monolayer titania films on SBA-15 supports are achieved with tuneable Ti content, confirmed by XPS (X-ray photoelectron spectroscopy), UPS (ultraviolet photoelectron spectroscopy), REELS (reflectance electron energy loss spectroscopy), ISS (ion scattering spectroscopy), and Raman analysis. XPS analyses reveal coverage-dependent Ti speciation, transitioning from isolated Ti atoms to interconnected Ti-O-Ti networks, with corresponding shifts in Auger parameters, indicating increased surface polarizability and Lewis acidity. Optimized Ti-SBA-15 catalysts exhibit a fourfold activity enhancement in photocatalytic activity over bulk TiO_2, attributed to improved mass transport, active site accessibility, and surface stability. This work highlights the potential of rationally designed hierarchical catalysts for scalable, energy-efficient biomass valorization into SAF precursors, offering a scalable, energy-efficient pathway for sustainable jet fuel production. By elucidating the structure-function relationships in sub-monolayer Ti-SBA-15 materials, this study provides critical insights for advancing photocatalytic technologies in renewable energy applications.

1. Introduction

Aviation represents one of mankind's greatest achievements, driving unprecedented economic and technological progress. This, however, comes at a cost. 2.5% of global carbon emissions result from air travel,[1] though non-carbon related activities, such as other emissions, and ozone reduction, have increased the effect on global warming to 4% since the industrial era.[2] Efforts to mitigate these impacts have led to the identification of low-carbon, and life cycle emission reducing feedstocks, with biomass emerging as a promising alternative. Lignocellulosic biomass is considered a second-generation (2G) feedstock and represents an extremely attractive option for the resourcing of carbon fuels, given its relative abundance and low cost,[3] production from waste sources, ease of implementation in sustainable circular economy strategies,[4] and non-competition with food sources.[5] 2G Lignocellulosic biomass sources are particularly exciting in the aviation sector, where liquid fuels are a requisite.[6] Catalysis plays a key role in the conversion of crude biomass feedstocks, into usable and high-value

M. A. Isaacs, A. Graf
HarwellXPS
Research Complex at Harwell
Rutherford Appleton Labs
Harwell Campus
Didcot OX11 0FA, UK
E-mail: mark.isaacs@ucl.ac.uk

The ORCID identification number(s) for the author(s) of this article can be found under https://doi.org/10.1002/adfm.202502818

DOI: 10.1002/adfm.202502818

M. A. Isaacs, S. Kroon, E. Garland
Department of Chemistry
University College London
Gower Street, London WC1H 0AJ, UK

M. A. Isaacs, S. Kumar
Diamond Light Source
Harwell Science and Innovation Campus
Didcot OX11 0DE, UK

C. Drivas, E. Garland, I. Lezcano-Gonzalez, C. M. A. Parlett
UK Catalysis Hub
Research Complex at Harwell
Rutherford Appleton Labs
Oxfordshire OX16 0FA, UK

chemicals in an energy efficient and selective fashion, and represent an enormously valuable technology for the valorization of biomass feedstocks into fuels and products.[7] Lignocellulosic biomass, composed of cellulose, hemicellulose, and lignin, is an excellent precursor for sustainable aviation fuel production. Through processes, such as enzymatic hydrolysis and thermochemical conversion, it can be transformed into platform molecules like furfural, 5-hydroxymethylfurfural, and levulinic acid.[8] These intermediates can undergo C—C coupling reactions (e.g., aldol condensation, ketonization, oligomerization) and oxygen removal steps (e.g., dehydration, hydrogenation) to produce jet fuel precursors with carbon chain lengths (C_8—C_{16}) suitable for aviation fuel.[9]

As such, the rational design of heterogeneous catalysts is of critical importance in the development of next-generation technologies, with numerous synthetic protocols available, forming a toolkit for the nanomaterials chemist to create and modify complex architectures to control catalytic behavior and activity.[10] Traditional catalysts, such as metal oxides (MgO, CaO, ZnO) and mixed oxides (Mg—Zr, Mg—Al), have shown potential in aldol condensation reactions.[11] However, their low surface areas and limited opportunities for surface modification restrict their usefulness. The use of metal alkoxides to modify an otherwise chemically unremarkable surface in silica, allows us to take advantage of the structural malleability of the material and imbue it with a degree of functionality, while maintaining catalyst thermal, chemical and mechanical stability.[12] This procedure is well-established[13] and has been used to both modify surfaces to improve the catalyst-support interaction of high surface area silicas,[13,14] and to control the locale of active sites within spatially segregated bifunctional catalysts.[15]

While the modification of the silica surface with TiO_2 sub-mono, and multi-layers has been studied in detail via deposition,[16] and alkoxide modification,[17] attempts to understand the TiO_2 growth modes on porous materials have been more scarce, particularly concerning an understanding at the sub-monolayer level that may present opportunities for defect-trapping chemistry[18] and advanced nanomaterial synthesis protocols such as strong electrostatic attraction deposition.[19] Knowledge of the chemical and spatial properties of deposited films, particularly in the sub-monolayer regime, will unlock new synthetic pathways and combinations of mixed oxide materials with finely tuned control over electronic properties. In this work, we use a gallery of surface science techniques to develop a holistic understanding of ultrathin titania films deposited onto a high surface area silica, in the sub-monolayer regime.

The conversion of biomass-derived cyclopentanone (CPO) and furfural (FAL) into C_{10}-C_{15} jet fuel precursors, 2-(2-furylmethylidene) cyclopentanone (FCp) and 2,5-bis(2-furylmethylidene) cyclopentanone (F_2Cp), is a key step in producing sustainable jet fuels from hemicellulose.[20] As outlined in **Scheme 1**, this process involves an initial aldol cross-condensation of furfural and cyclopentanone to form the 4-(furan-2-yl)-4-hydroxycyclopentone (FCp-OH) intermediate. This intermediate then undergoes rapid dehydration to yield FCp. FCp can subsequently participate in a second aldol condensation with furfural to form the final C_{15} product, F_2Cp. The aldol condensation of furfural with ketones is known to proceed as a thermally-driven acid-catalyzed process,[20] or through photoactivation, with solid acid catalysts enabling the coupling of CPO and FAL. TiO_2 has been identified as an active and tunable catalyst for furfural-ketone aldol condensations to form F_2Cp.[21] While parts of this mechanism are industrially established,[22] ongoing research focuses on scaling and optimizing the remaining steps to achieve commercial viability.[23] To the best of the authors' knowledge, the photocatalytic conversion of FAL and CPO to F_2Cp has yet to be demonstrated.

Despite the extensive use of grafted Ti-SBA-15 as a solid Lewis acidic catalyst support, its coverage-dependent catalytic activity (and associated in-depth mechanistic understanding) remains poorly understood. Here, we report the first application of solvent-free, photocatalyzed aldol cross-condensation of cyclopentanone with furfural, using Ti-SBA-15 catalysts synthesized by alkoxide hydrolysis. Controlled Ti overlayer growth over silica architectures led to enhanced mass-transport and active site accessibility characteristics (over bulk TiO_2 catalysts), with strict control of Ti surface coverage imparting fourfold enhancements in photocatalytic activity and enhanced catalyst stability.

2. Results and Discussion

2.1. Material Properties

Successful preparation of the parent SBA-15 support confirmed via SAXS (small angle X-ray scattering) and N_2 porosimetry measurements (Figure S1, Supporting Information), with the measurements indicating a *P6mm* type pore symmetry, a Type

C. Drivas
Cardiff Catalysis Institute
School of Chemistry
Cardiff University
Cardiff CF10 3AT, UK

C. Drivas, A. Graf
School of Chemistry
Cardiff University
Park Place, Cardiff CF10 3AT, UK

J. Liu
Department of Chemistry
Imperial College London
Exhibition Road, South Kensington, London SW7 2AZ, UK

A. Torres-Lopez
Cornell High Energy Synchrotron Source
Wilson Laboratory
Cornell University
Ithaca, NY 14853, USA

C. Price, I. Lezcano-Gonzalez, C. M. A. Parlett
Department of Chemical Engineering
University of Manchester
Manchester M13 9PL, UK

I. Lezcano-Gonzalez
Diamond Light Source
Harwell Science and Innovation Campus
University of Manchester at Harwell
Didcot, Oxfordshire OX11 0DE, UK

V. C. dos Santos-Durndell, L. J. Durndell
School of Geography
Earth and Environmental Sciences
Faculty of Science and Engineering
Plymouth University
Plymouth PL4 8AA, UK
E-mail: lee.durndell@plymouth.ac.uk

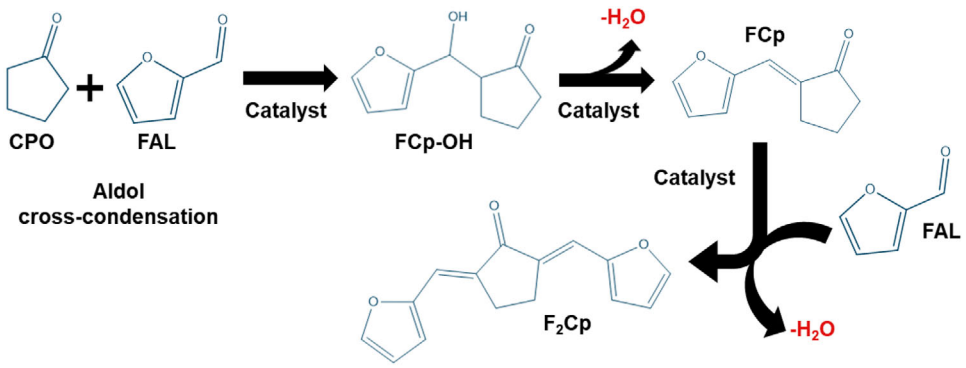

Scheme 1. The solvent-free production of F_2Cp from furfural and cyclopentanone.

IV isotherm and H2 hysteresis, characteristic of SBA-15. DFT pore size distributions revealed a marginal decrease in average pore diameter with increasing sub-monolayer coverage, indicating pore wall coating (Figure S2, Supporting Information). Surface area marginally decreased with coating, particularly in the micropore domain suggesting monolayers coatings block micropore openings (Table S1, Supporting Information). Grafted sub-monolayers of TiO_x were prepared with a varying fractional surface coverage (θ) between 0.2 and 1, determined from calculating the total number of silanol groups on the SBA-15 surface, assuming a silanol density of 0.6 OH.nm^{-2}, and the molar amount of Ti precursor added to produce the desired surface coverage. Since the hydrolysis and condensation process is performed in anhydrous toluene, the reaction should proceed only via surface silanols, and be self-limiting in nature. SEM (**Figure 1**a,b) and TEM (Figure S3, Supporting Information) confirmed the absence of large amorphous particles of non-porous titania, which may be formed via moisture contaminations causing immediate hydrolysis and self-condensation while EDX determined the titanium metal loading (Table S2, Supporting Information). Due to the nature of these ultra-thin monolayers of titania, XRD is an unsuitable probe into the local structure of the films (Figure 1d), reporting an amorphous structure only. Raman spectroscopy, however, indicates an anatase phase for the TiO_2 moieties (Figure 1c).[24]

XPS presents an ideal tool by which to probe these systems, given the inherent surface sensitivity of the technique and compatible size regime of these ultra-thin films and the information depth. Initial quantification of the resultant spectra revealed

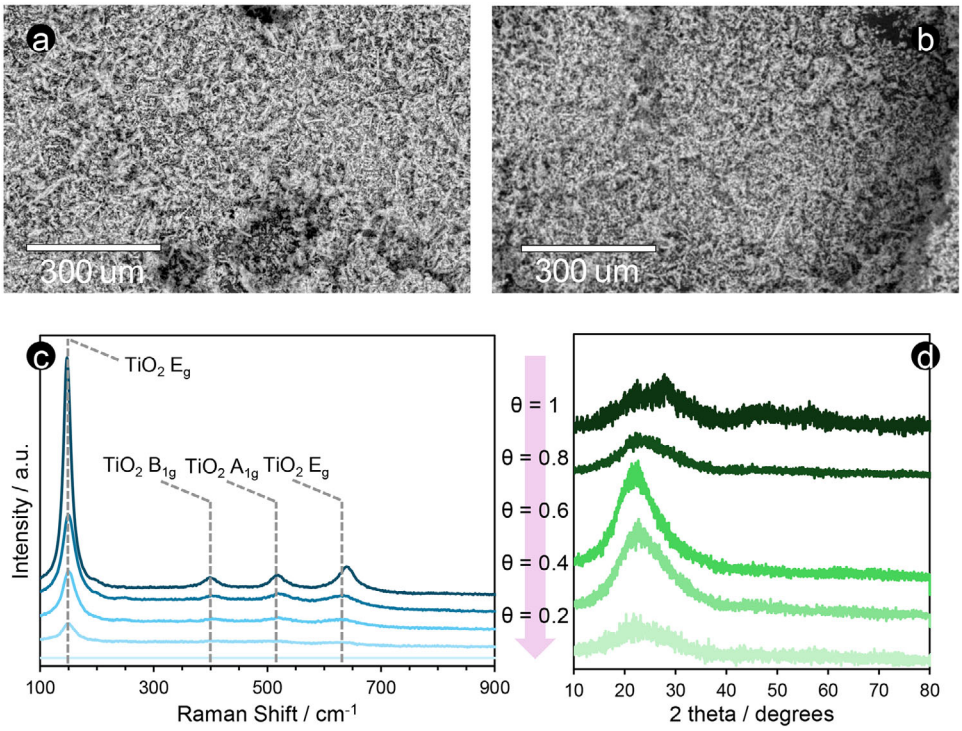

Figure 1. Representative SEM images of a) 0.2θ, and b) 1θ fractional surface coverage Ti on SBA-15, c) Raman spectra, and d) XRD diffractograms of all five fractional surface coverages of ultra-thin Ti films prepared.

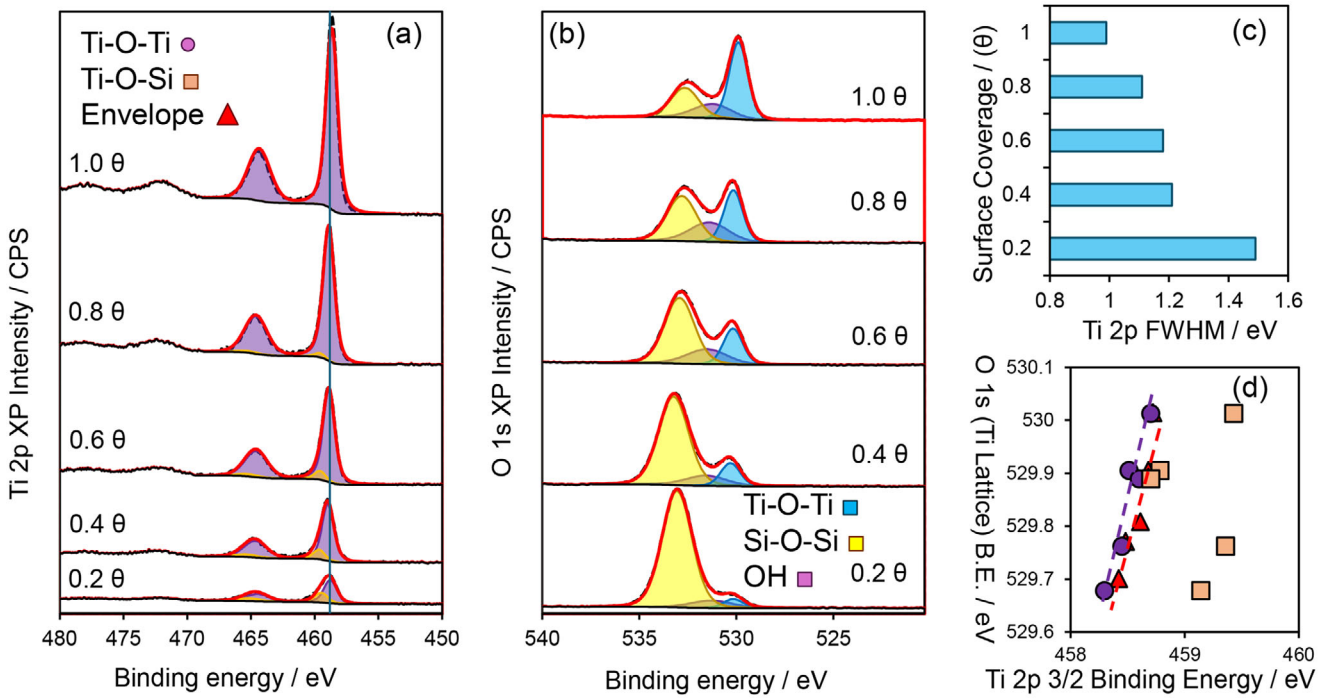

Figure 2. Deconvoluted a) Ti 2p, and b) O 1s XP spectra, c) FWHM of Ti 2p peaks as a function of fractional surface coverage, and correlation plots of Ti $2p_{3/2}$ binding energies for Ti—O—Ti, Ti—O—Si components, and total envelope, versus O 1s lattice oxygen binding energy (Ti).

a trending relationship between carbon contamination content versus fractional surface coverage of titanium (Figure S4, Supporting Information). Carbon overlayer coating thickness was calculated, and the atomic contents corrected for the overlayer attenuation of photoelectron peaks of different kinetic energies (Table S2, Supporting Information) using the Smith method,[25] and TPP2M calculations.[26] XPS revealed the presence of no elements other than Ti, Si, O, and C, and indicated an increasing Ti content with Ti loading along with a concomitant decrease in silicon signal (Figure S5a, Supporting Information). Ti content scales linearly with both theoretical surface coverage and bulk loading (Figure S5b, Supporting Information), suggesting that the grafted films could be growing in the expected layer-by-layer (LbL) fashion, due to the self-limiting nature of the anhydrous alkoxide hydrolysis and condensation process, and offering supporting evidence of a lack of formation of bulk TiO_2 particles away from the SiO_2 surface. At the maximum Ti loading, we find a coverage of ≈3.3 Ti atoms nm^{-2}, based on calculations of Ti content from EDX analysis and the silica surface area. This is slightly below the reported "monolayer formation" coverage of 4 atoms nm^{-2} for TiO_2 on silica,[17] attributed to silanol coverage differences. Ti 2p spectra were found to broaden with decreasing fractional surface coverages (**Figure 2c**), and as such were modeled with a separation of two individual components – one using the peak model parameters of the "complete" film (where $\theta = 1$), and another based on the differential spectra between high and low surface coverage, which indicated the presence of a secondary species at higher binding energy (Figure 2a). Differences in surface speciation of ultrathin films have been observed previously,[27] and two species were identified as individually situated Ti atoms bound through Si—O—Ti bonds (lower binding energy), and regions of larger complete layer formation (e.g., networks of Ti—O—Ti, atop the silica surface, bound through Si—O—Ti linkages) that dominate the higher surface coverages (lower binding energy).

The O 1s region was deconvoluted into the two lattice oxygens for TiO_2 (530 eV) and SiO_2 (532.7 eV), and a third species denoted as OH (531.3 eV) (Figure 2b), based on modeling of standard reference materials of TiO_2 anatase. To further probe the assignments of the Ti and O deconvolutions, high-resolution Si 2p, Ti $L_3M_{4,5}M_{4,5}$, and O $K_1L_{2,3}L_{2,3}$ spectral regions were analyzed (Figures S6–S8, Supporting Information). Correlating the binding energy of related atoms within a component system is a method that has recently been investigated by Bhatt et al.[28] and offers a sanity check, free from any issues relating to sample charging or calibration, for spectral assignments in a series of related data, and may be considered a more robust appreciation of the data than simple binding energy analysis alone. Si 2p regions were deconvoluted into the corresponding Si—O—Si, and Si—O—Ti interfaces, and the respective binding energies plotted against the O 1s (Si—O, and OH) energies (Figure S9, Supporting Information). Only the Si—O—Si (Si 2p and O 1s) energies indicated any kind of correlation, indicating that our oxygen atoms with any Si—O—Ti linkages may not be resolved in our O 1s model, likely due to significant overlaps with the "OH" component within the model. For comparison, the overall binding energies of the Si 2p envelope, and O 1s peak were plotted, and revealed a significantly worse trend than the deconvoluted system, indicating that our model is more reflective of the system when we include the twin environment peak component system, rather than assume a singular species suffering peak broadening alone. This process was performed for Ti 2p also (Figure S10,

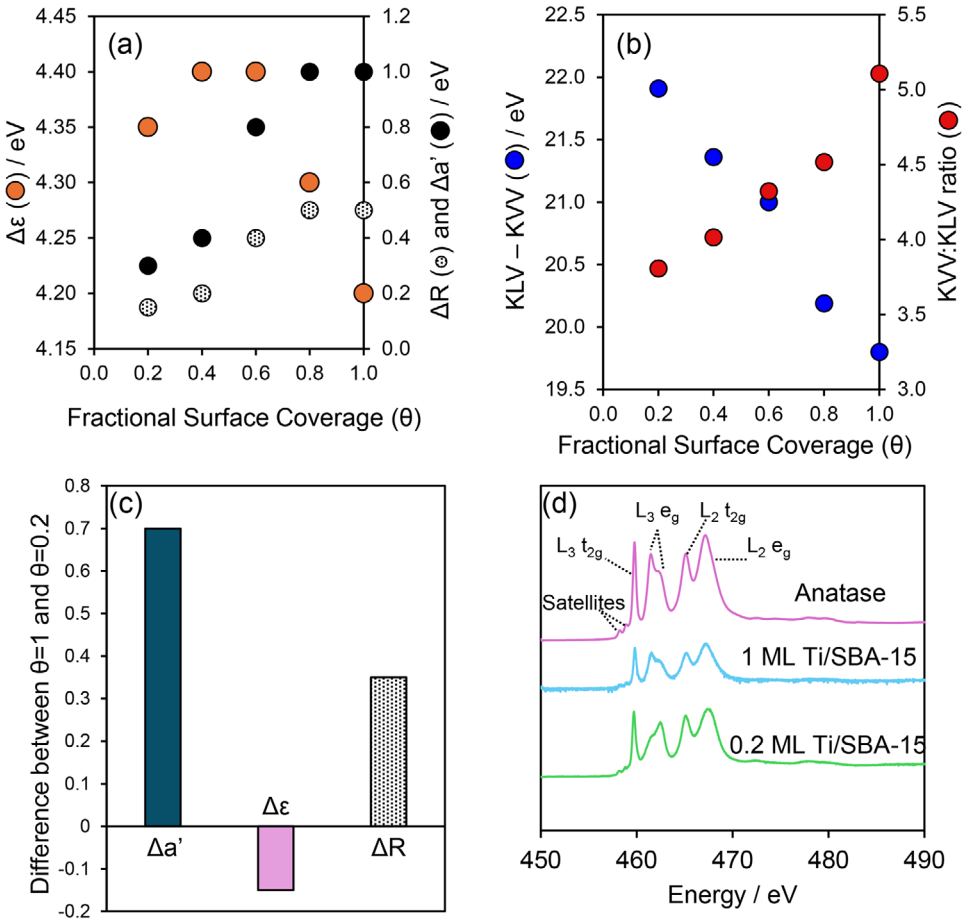

Figure 3. a) Auger parameter shift, and initial and final state contributions as a function of fractional surface coverage, b) O $K_1L_{2,3}L_{2,3}$ and $K_1L_1L_{2,3}$ peak area ratio and energy separation, c) enhancement or reduction of auger parameter shift, initial, and final state contributions when increasing fractional surface coverage from 0.2 to 1, d) Ti $L_{2,3}$ XANESX (X-ray absorption near edge spectroscopy) of anatase, 0.2, and 1 θ coverage.

Supporting Information), and again a good relation was found only for the Ti—O—Ti versus O 1s (Ti) systems. A comparison of the Ti—O—Si, Ti—O—Ti, and Ti spectral envelope can be found in Figure 2d.

Additional detail into the surface chemistry was provided by analysis of the Ti LMM and O KLL auger regions. Modified Auger parameters can serve as an indicator of changes in the polarisability of Ti centers,[29] which in turn will impact the Lewis acid nature of these sites. Analysis of the titanium auger parameter ($2p - L_2M_{2,3}M_{4,5}$) was broken down into initial and final state relaxation energies (**Figure 3**a–c) using the relationships in Equations S1–S3 (Supporting Information). As titania approaches monolayer coverage, the Auger parameter shift and final-state contributions increase, while initial-state contributions remain mostly consistent, with a slight decrease at higher surface coverages, indicating a more ionized, highly polarizable system.[30] This aligns with our model, where isolated Ti atoms at low surface coverage transition into larger monolayer regions at higher coverage. At sub-monolayer levels, the initial-state relaxation energy shifts negatively, while the final state shifts positively, suggesting more covalent-type Ti bonding. This likely arises from isolated titania centers with fewer bridging oxygen sites (and opportunities to form such species) between Ti atoms.

Surface polarizability (leading to surface acidity implications) can be explored by monitoring changes to the O 1s – O KLL a' of metal oxides.[31] Given that these systems are a mixed oxide, it is imperative that an accurate deconvolution of oxygen 1s photoemission states and KLL auger peaks be performed, though this is not a trivial process. The O 1s photoemission peak provides clear deconvolution yielding clear energy separation between lattice oxygen within SiO_2 (532.8 eV) and TiO_2 (530.0 eV) (Figure 2b). The KLL auger was deconvoluted using an empirical model derived from the analysis of unmodified SBA-15 and compared with the highest loading TiO_2 functionalized material ($\theta = 1$), enabling deconstruction of the complex auger structure into segmented O KLL (Si) and O KLL (Ti) regions, via non-linear least squares fitting (Figure 3d). Using these deconstructions and the fitting from the O 1s region, auger parameters have been calculated for both the Si-coordinated and the Ti-coordinated oxygen centers (Figure S11, Supporting Information). The surface polarizability of the titania component remains largely unchanged, save for a subtle increase for the highest loading material, suggesting little difference in Lewis acid/base site character across the series. The Si component may be used as an indicator of the interface between Si- bulk and Ti- overlayers. At low Ti loading, there is little change in the observable energetics of the Si atoms, until a surface

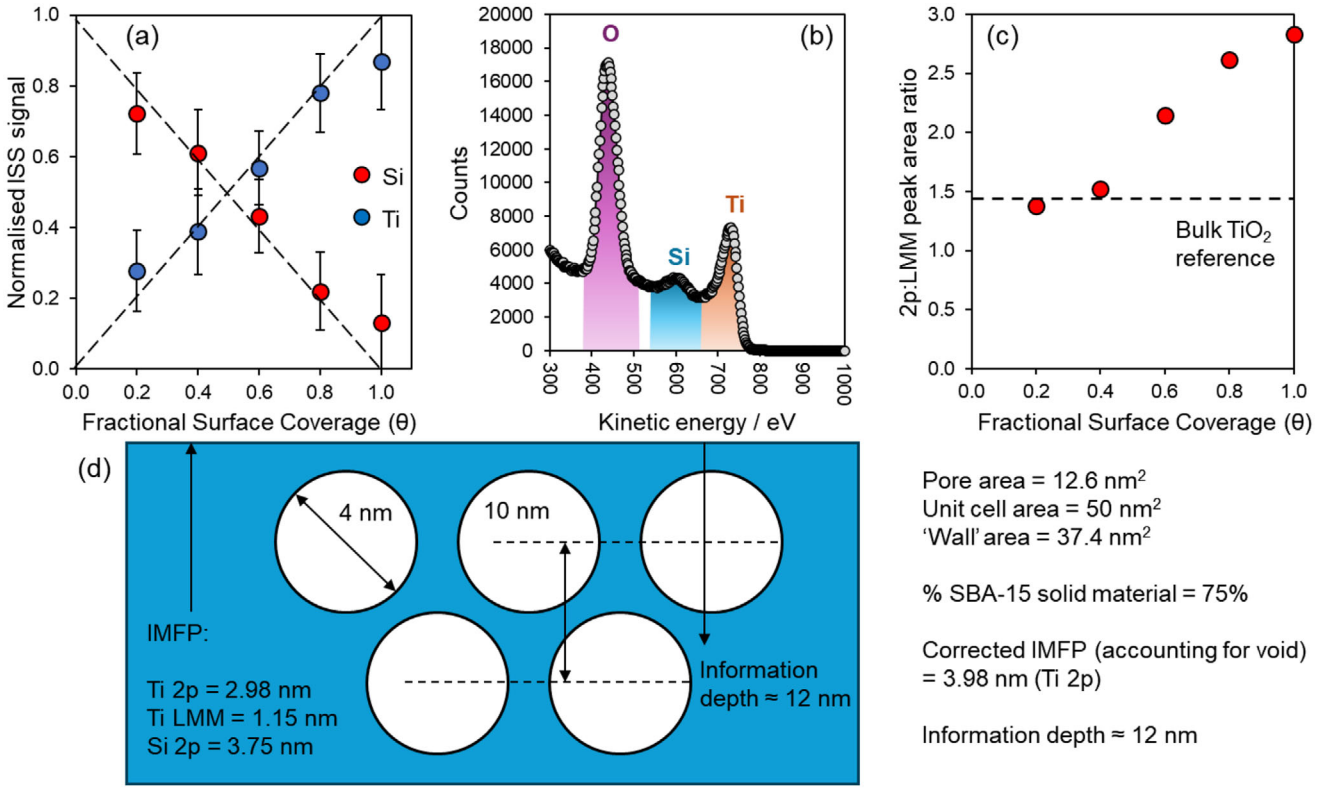

Figure 4. a) Normalized ion scattering spectroscopy intensities for Si versus Ti, b) representative ISS spectrum of θ = 1.0 Ti on SBA-15, c) intensity ratios for Ti 2p core level photoelectrons, versus Ti LMM auger electrons as a function of surface coverage, d) mean free paths and information depths proposed for porous mixed oxide system.

coverage of ≈0.8θ, at which point a minor reduction in the auger parameter is observed, indicating a decrease in polarizability. It is likely that at lower Ti loading, this property is simply dominated by bulk-like Si. It is not until we reach this threshold of 0.8θ that the impact of forming Ti—O—Si linkages diminishes the Lewis base strength of the O lone pairs due to the induced dipole formation from the introduction of a more electropositive titanium center to the oxygen linker. This observation provides further evidence for the formation of chemically bonded Si—O—Ti species, rather than deposition of discrete Ti nanoclusters. In order to correlate these measurements with more substantial insights into the surface acidity, ammonia TPD was performed on the five fractional Ti surface coverages (Figure S12, Supporting Information). Overall, all materials exhibited a similar profile, with only the 0.2 θ material deviating significantly. The traces were deconvoluted into weak (≈180 °C), medium (≈230 °C) and strong (≈330 °C) sites in order to fit the desorption profile, as has been reported for similar materials previously.[32] Isolating the major acid site type present on these materials (medium strength), we see a trend with surface coverage of decreasing desorption temperature with increasing surface coverage. This indicates marginally weaker acid sites, in line with our XPS interpretations.

Ti K-edge XANES was performed on an anatase reference material and compared with the 1θ monolayer coverage sample (Figure S13, Supporting Information). The composite material indicated the typical features of a TiO_2 polymorph, however, due to the low loading of Ti, little additional data could be extracted. To further probe the titanium environment, Ti $L_{2,3}$ XANES was employed (Figure 3d) for the lowest and highest coverages and compared against an anatase reference. Both composites exhibited the expected peak splitting, and relative broadening between L_2 and L_3 peaks due to Coster–Kronig auger decay for the L_2 peaks.[33] The titanium was observed to be in octahedral symmetry in both samples – with t_{2g} and e_g peaks both present due to crystal field splitting, however the low coverage composite revealed a reversed intensity ratio between the two L_3 e_g peaks, along with a slightly lower energy L_3 t_{2g} peak – both indicative of rutile phase TiO_2,[34] suggesting the local environment of these ultralow coverages differs significantly from the more complete monolayers. This is our first insight into the symmetry of these very small clusters of surface-grafted TiO_2, and may be used to influence sophisticated multistep synthesis of complex nanoarchitectures.

Resolving spatial information about the deposited films remains a crucial aspect of understanding the synthesis, and eventual materials. Insight into the topological material properties was investigated by ion scattering spectroscopy (**Figure** 4a,b), to probe the terminal surface. Ion scattering trends will not identify titania within the pores, instead probing only the outer 1–2 atomic layers. Again, a linear trend between the ISS Ti peak area and theoretical surface loading is observed, further suggesting the capped layer growth model of a self-limited condensation (and lack of self-hydrolysis and condensation when using the

anhydrous conditions employed). There is a possibility that we observe a marginally increased Ti composition at low fractional surface coverages than we might expect, though this is mostly within the error of the measurement. That this trend matches that of the Ti 2p XPS is suggestive of comparable growth modes both inside the pores and on the outer surface, since by our calculations the Ti 2p emission probes above an entire layer of pores if we assume the worst-case scenario of the pores lying perpendicular to the angle of emission (Figure 4d). Realistically, the nature of powder samples means that random angles of pore alignment only serve to further increase the effective information depth of inner-pore emissions – since pore close to the parallel (i.e., pointing vertically upward) will inhibit electron transport to a lesser degree than those lying perpendicular.

The large difference between kinetic energies of the Ti 2p and Ti LMM emissions when excited using standard laboratory sources gives us a secondary method by which to assess spatial parameters, since the information depths through bulk TiO_2 vary wildly (21.32 Å v 11.16 Å). If we assess the intensity ratio (after carbon correction, according to the aforementioned Smith method)[25] between the Ti 2p photoelectrons (which favors quantification of deeper lying, inner pore coatings), and the Ti LMM auger electrons (which will be dominated by the external surface), we see that this ratio varies to a significant degree upon increasing fractional surface coverage (Figure 4c). This observation is crucial for the design and development of complex, spatially segregated materials, since it implies a degree of hindered diffusivity of alkoxide molecules, and a preference for grafting at the external surface rather than the inner pore walls, during initial synthesis. This may be utilized to reduce synthesis steps in the production of such materials, particularly in the case of using an alkoxide with larger, sterically hindered ligands (e.g., *tert*-butoxides), indicating the possibility to spatially direct surface modifiers using intrinsic diffusivity differences alone.

Nanomaterial electronic properties were probed by REELS, UPS and UV–vis spectroscopies. First, REELS (Figure S14, Supporting Information) was utilized to determine material bandgap,[35] and permitted a degree of deconvolution due to the distinct regions of scatter from TiO_2 (bandgap ≈3.5 eV) versus SiO_2 (bandgap ≈8.9 eV) as evidenced by the large separation between the primary scatter features in the REELS analyses. A clear trend is observed from 3.75 eV (0.2θ) down toward a bulk-like TiO_2 bandgap, with $\theta = 1$ reporting a bandgap of 3.55 eV, close to that recorded for the P-25 reference material. This highlights the potential of sub-monolayer titania as a source of bandgap tuning for advanced heterojunction composite systems and, in conjunction with a low bandgap material such as copper (II) oxide, may offer an exciting route toward optimization of excited state stabilization for solar spectrum initiated photocatalysts. This trend in decreasing bandgap as we approach a monolayer coverage correlates with DRUVS measurements (Figure S15, Supporting Information), agreeing with previous observations made on amorphous silica substrates.[17] Notably, bandgap values determined by REELS appear slightly higher than those determined by DRUVS, likely due to DRUVS measuring the lowest energy threshold for exciton formation, whereas REELS measures the bandgap as the separation between the valence and conduction bands.[35] This subtle difference highlights the complementary data provided by REELS analysis, and lends itself toward building a greater understanding of the energetic structure of photolytically active materials.

Furthermore, UPS reveals a secondary trend wherein both the material work function and valence band maximum (VBM) span a relatively wide range as they transition toward bulk-like TiO_2 (Figure S16, Supporting Information). Even at the highest Ti surface coverage, the valence-band maximum (VBM) sits above that of bulk TiO_2, probably because the surface is dominated by interface-type Ti centers (Ti–O–Si). Reducing the surface coverage, thereby generating smaller TiO_2 domains, widens the bandgap and shifts the VBM to more negative potentials relative to vacuum, behavior characteristic of quantum-confinement effects.[36] This, combined with REELS-determined bandgaps, further serves to highlight the exciting electronic level tuneability of these systems, with the potential to permit highly advanced coordination of energy levels when used in conjunction with a secondary photocatalytically active moiety.

2.2. Photocatalytic Activity and Mechanism

The aldol cross-condensation of cyclopentanone and furfural was investigated over a series of Ti-SBA-15 catalysts under solvent-free conditions, evaluating catalytic activity under visible and UV light (365 nm). Analogous studies using rutile, anatase, P-25, and unfunctionalized (parent) SBA-15 were conducted for benchmarking purposes. GC-MS analysis confirmed the formation of FCp-OH, FCp and F_2Cp as the main reaction products. Negligible humin formation, as a result of cyclopentanone or furfural self-condensation, was observed across all tested conditions, including variations in catalyst mass, reaction time, light source (UV/visible), and during recycling studies. This indicates effective suppression of polymeric side-products under the applied photocatalytic conditions. A blank experiment was also conducted in the absence of catalyst (under visible and UV light exposure), which resulted in negligible conversion of either reactant.

All titania materials exhibited activity under both UV and visible light regimes, while the parent silica, lacking Lewis acid sites, showed negligible furfural conversion (Figure S17, Supporting Information), indicating that while this reaction is primarily driven by Lewis acid sites, the process may be enhanced photolytically. Rutile outperformed anatase under visible light, while both phases exhibited similar activity under UV light. This difference is likely due to the higher density of Lewis acid sites on rutile phase TiO_2,[37] compensated for by the superior photocatalytic activity of anatase phase TiO_2.[38] Although UV–vis absorption spectra were not directly measured in this study, literature reports show that cyclopentanone absorbs primarily below 300 nm, and furfural only weakly beyond 340 nm, with both exhibiting negligible absorption at 365 nm.[39] The intermediates, FCp and FCp-OH, are likely to absorb only in the deep UV based on their proposed structures and are present at low steady-state concentrations due to their transient nature. Under 365 nm irradiation, reactant direct excitation or self-sensitization is therefore unlikely. The observed photoactivity is attributed to the photocatalyst as the primary light-absorbing and reactive species, further supported by the absence of reactant degradation in control experiments without catalyst, and at high conversions (>50%), where

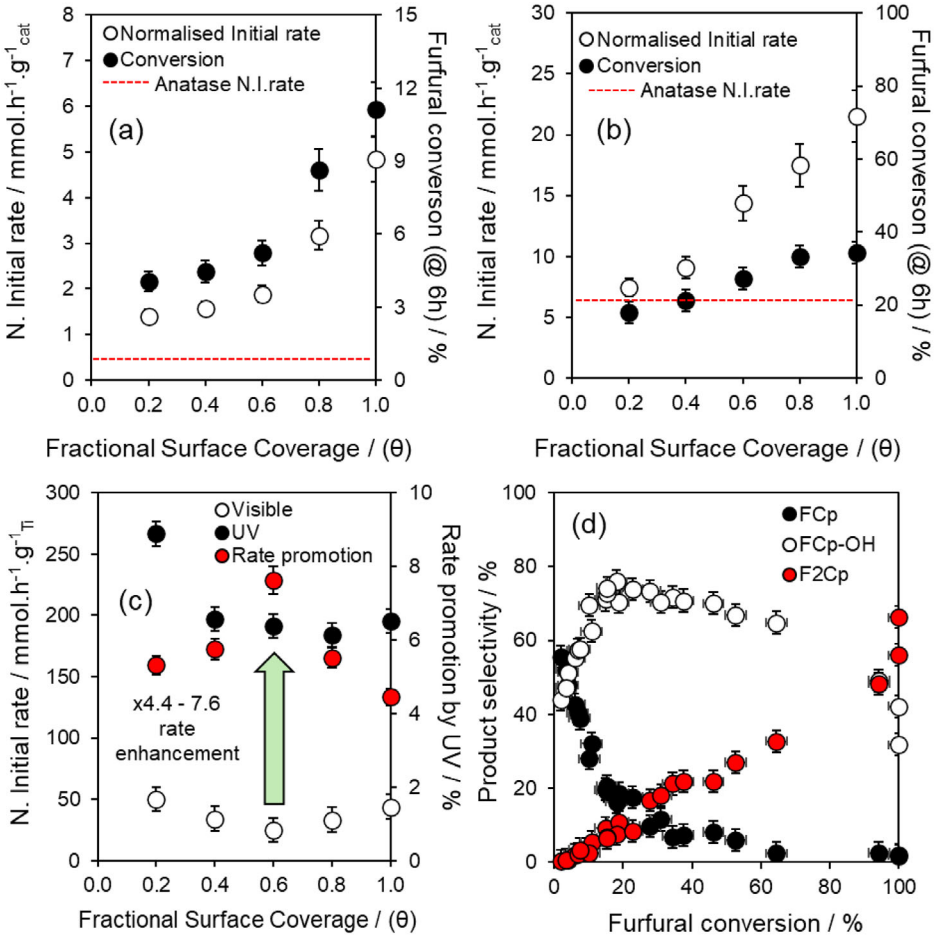

Figure 5. Normalized initial rates and conversions for all prepared ultrathin film samples under a) visible light, and b) UV (365 nm), c) normalized initial rates per mass of titania for all prepared ultrathin films; d) Product selectivity as a function of furfural conversion (across all experiments). Reaction conditions: 80 °C, 10 mmol furfural, 30 mmol cyclopentanone, a–c) 0.05 g catalyst, d) 0.025–0.200 g catalyst, 800 rpm.

UV-mediated degradation products were not detected. Future time-resolved or in situ spectroscopic studies could provide further insight into the photophysical roles of the intermediates.

Films prepared from Ti-SBA-15 demonstrated superior activities when under visible light, compared to the bulk P-25 and associated anatase and rutile TiO_2 bulk phase references (Figures S17 and S18, Supporting Information). This enhanced performance is attributed to their substantially larger surface areas (500–700 m^2 g^{-1} vs 30–50 m^2 g^{-1}) and elevated hydroxyl group surface concentrations, as confirmed by N_2 porosimetry and XPS analyses, respectively (Figure S2, Supporting Information; Figure 2b). Surface hydroxyl groups have been shown to facilitate aldol condensation via solid base-catalyzed enolate formation.[21]

Previous studies report that bulk TiO_2, lacking Brønsted acid sites and relying on weak Lewis acid sites, shows limited ability to catalyze FCp-OH dehydration to FCp.[40] Photoirradiation overcomes such limitations by generating electron–hole pairs, which significantly enhance Ti Lewis acid site performance for efficient FCp-OH conversion. Under UV irradiation (**Figure 5b**), all materials demonstrated pronounced activity increases, with tunable two to sevenfold rate improvements. Notably, bulk anatase exhibited the greatest enhancement (>7-fold) compared to rutile and P-25 (1-2-fold), likely due to its superior efficiency in generating core holes.[41] Normalizing for catalyst mass (Figure 5a–c) showed increasing conversion and initial rate with higher fractional Ti surface coverage, attributed to greater titania surface concentration. However, initial rate normalization per unit mass of titania (or surface density) revealed a relatively consistent performance across the series, except for the lowest surface coverage ($\theta = 0.2$), which outperformed the higher Ti loadings (potentially owing to the increased acid site strength for this material, and alternate Ti center symmetry as observed by NEXAFS). This enhanced performance, coupled with the highest bandgap and lowest surface polarizability characteristics, suggests an initial preferential deposition of titania species on the external surface of the silica framework during synthesis. Such deposition likely minimizes reactant-product diffusion limitations within the mesoporous network, thereby enhancing catalytic efficiency. As Ti surface concentration increases beyond sub-monolayer coverage, internal mesopore deposition becomes dominant, promoting uniform Ti distribution, but compromising reactant-active site mass-transport kinetics, when compared to sub-monolayer samples ($\theta < 0.5$).

Product distribution profiles across all catalytic experiments (Figure 5d; Figures S19 and S20, Supporting Information), support a stepwise reaction sequence for the formation of FCp and F_2Cp, whereby FCp-OH, generated during initial aldol cross-condensation between photoactivated furfural and cyclopentanone, undergoes Lewis acid-catalyzed dehydration to FCp. High [FCp-OH] is required to drive this process, with a first-order dependence between catalyst mass and furfural conversion further highlighting the conversion-dependant nature of this reaction (i.e., increased catalyst mass enhancing FCp and F_2Cp production). Secondary aldol cross-condensation of FCp to F_2Cp proceeds with near-quantitative efficiency, scaling linearly with furfural conversion (and surface Ti concentration). This suggests the presence of a structure-insensitive process operating under low reactant coverage, characterized by weak adsorption or rapid reaction kinetics, with initial FCp generation being the rate-limiting step in this catalytic cascade.

Mechanistically, we propose that the photocatalytic cascade proceeds via photoinduced generation of reactive radical intermediates on the Ti-SBA-15 surface. Upon UV irradiation, electron–hole pairs form within the dispersed TiO_2 domains. Photogenerated holes (h^+) oxidize furfural to form a radical cation (FAL$\bullet^+$), which rapidly deprotonates to create a resonance-stabilized furyl radical. Concurrently, photogenerated electrons (e^-) reduce cyclopentanone to a cyclopentanonyl radical anion, which undergoes hydrogen atom transfer to produce a neutral radical. The coupling of these two carbon-centered radicals yields the mono-condensed intermediate FCp-OH, which then undergoes Ti Lewis acid-catalyzed dehydration to form FCp. A second photoinitiated furfural activation enables further condensation with FCp to generate F_2Cp. While photoexcitation is essential for radical generation (a process favored under UV irradiation at 365 nm), the subsequent coupling and condensation steps are likely thermally driven. This behavior mirrors phenomena observed in the photocatalytic oxidation of benzyl alcohol to benzaldehyde over Ti-based photocatalysts[42] wherein efficient charge separation and surface radical formation govern both activity and selectivity.

XRD and ICP-MS analysis of post-reaction catalysts and reaction media showed negligible Ti phase sintering (Figure S21 and Table S3, Supporting Information), and minimal Ti leaching. Catalyst stability was assessed via recycle experiments using the θ = 1 Ti-SBA-15 catalyst (Figure S22, Supporting Information). Spent catalysts were recovered by filtration, washed with ethyl acetate, and reused for two additional reaction cycles with fresh reaction mixtures. After three cycles, no significant deactivation was observed, with furfural conversion (6 h), initial rates, and product selectivity values remaining consistent across cycles.

The observation that this reaction may be activated photolytically is an exciting development in sustainable aviation fuel production, and investigations into the individual impacts of Lewis acid site strength/density, core-hole stability, bandgap, and diffusion kinetics will be the next step in revealing the viability of these materials for large scale application.

3. Conclusion

This work highlights the highly tunable nature of sub-monolayer ultrathin films, both in their chemical and electronic properties and in their preferential adherence to porous architectures. These observations will enable finely tuned, bespoke nanomaterial systems, and advance the toolkit for the nanomaterials scientist for the development of complex, multifunctional nanostructures. Catalyst performance was evaluated as photoactivated, Lewis-acid catalysts for the conversion of biomass-derived feedstock molecules into high-value, sustainable aviation fuels. Grafted ultra-thin films outperformed bulk materials, with photoactivation enhancing film catalytic activity by up to fourfold. Increased acid site activity for low Ti coverages (and by extension any acidic, graftable species (i.e., Al, Ce, Zr)) may present an interesting avenue for catalyst optimization when combined with thicker, photocatalytically active films, providing the best of both worlds to promote product formation.

This reaction presents an opportunity to explore how spatial preferences can be used to develop new catalyst nanomaterials that favor specific reaction pathways. The bulky nature of products like F_2Cp, along with sterically challenging side products (e.g., humins), contrasts with smaller reactants, offering key insights for designing new catalysts that suppress side product formation. For example, steric hindrance within (and around) mesopores could reduce side reactions at higher temperatures or increased furfural concentrations. Additionally, the potential to generate cyclopentanone directly from furfural opens the possibility of simplifying the process by using a fully furfural-based feedstock with the appropriate catalytic strategy.

4. Experimental Section

Materials: SBA-15 was prepared using a cooperative self-assembly method,[24] in which a 2.6 wt.% solution of Pluronic P123 triblock copolymer (poly(ethylene glycol)-poly(propylene glycol)-poly(ethylene glycol) (Sigma–Aldrich), in 1.6 M HCl solution was stirred (500 rpm) at 35 °C. Tetraethyl orthoxysilicate (Sigma–Aldrich, 98%) was then added to the mixture, at a molar ratio of 60:1 [TEOS]:[P-123]. The mixture was aged at 80 °C for 24 h without stirring in a sealed container in an oven. The resultant solid material was filtered, then washed with ethanol before drying in air at 100 °C overnight. P123 framework removal was performed by calcination at 500 °C in a muffle furnace for 6 h with a ramp rate of 1 °C min^{-1}.

Titania grafting onto the surface of the prepared silica materials was conducted using a modified procedure by Landau et al.[43] in which triethylamine is used to activate the surface silanols on the silica, allowing the reaction to proceed at lower temperatures. To ensure uniform TiO_2 coating, the reaction must be performed under completely dry conditions, due to the facile hydrolysis of the titania precursor, which readily forms large titania particles in the presence of water. The synthetic procedure involves mixing titanium isopropoxide (Sigma–Aldrich,) in anhydrous toluene (Aldrich, water content <0.002%), adding triethylamine (Sigma–Aldrich, >99%) and MM-SBA-15 or SBA-15 material whilst stirring at 85 °C for 6 h under nitrogen flow. The concentration of titanium isopropoxide was 145 g L^{-1}, the molar ratio between titanium isopropoxide and SBA-15 was varied to control surface coverage and the triethylamine: SBA-15 weight ratio at 1.5 on a scale of 5 g of SBA-15. After the reaction, the solid was separated by filtration, washed with toluene (300 mL) and inserted in a 0.5 wt.% water-ethanol solution (500 mL) under stirring for 24 h. The resultant solid was washed with ethanol, dried in air in an oven at 90 °C for 24 h, then calcined for 1 h at 250 °C, 1 h at 400 °C and finally for 4 h at 500 °C. Ramp rates of 1 °C min^{-1} used throughout.

Characterization: XPS, UPS, REELS, ISS, and Raman Analysis was performed using a Thermo NEXSA XPS fitted with a monochromated Al k_α X-ray source (1486.7 eV), a spherical sector analyzer and three multichannel resistive plate, 128 channel delay line detectors, a He(I) (21.22 eV) UV

lamp, a MAGCIS ion gun, a low energy electron gun, and an iXr coincident 455 nm Raman laser. XPS data was recorded at 72 W and an X-ray beam size of 400 × 200 µm. Survey scans were recorded at a pass energy of 160 eV, and high-resolution scans recorded at a pass energy of 20 eV. Electronic charge neutralization was achieved using a Dual-beam low-energy electron/ion source (Thermo Scientific FG-03). Ion gun current = 150 µA. Ion gun voltage = 45 V. All sample data recorded below 10^{-8} Torr and pressure and a room temperature of 294 K. The instrument was calibrated to gold metal Au 4f (83.95 eV) and dispersion adjusted to yield a binding energy (BE) of 932.6 eV for the Cu $2p_{3/2}$ line of metallic copper. Ag $3d_{5/2}$ line FWHM at 10 eV pass energy was 0.5 eV. Source resolution for monochromatic Al Kα X-rays is ≈0.3 eV. The instrumental resolution was determined to be 0.36 eV at 10 eV pass energy using the Fermi edge of the valence band for metallic silver. Resolution with charge compensation system on <1.4 eV FWHM on PTFE. Data was analyzed using CasaXPS v2.3.19PR1.0. Peaks were fit with a Shirley background before component analysis. Line shapes of LA (1.53243) were used to fit components. UPS spectra was recorded using a sample bias of 9 V, and samples were dropcast onto a gold foil before measurement, according to the method of Maheu et al.[44] REELS analysis was performed with a 1 keV electron beam. ISS was performed with a 1 keV ion beam, and a raster area of 1 mm^2. Raman analysis was performed using a 455 nm laser source operating at 5 W power. Scanning electron microscopy with energy dispersive X-ray spectroscopy (SEM-EDX) was performed using a Thermo Phenom SEM with dispersive EDX detector. Diffuse reflectance UV–vis spectroscopy (DRUVS) was performed using a Shimadzu UV2600 integrated sphere spectrometer. Data was recorded in absorbance with a step size of 0.5 cm^{-1}. Small angle X-ray scattering (SAXS) scattering patterns were obtained on Xenocs Nano-inXider, equipped with microfocus sealed tube: Cu, 30 W =, point focus. With Dectris Pilatus 3 hybrid photon counting (two fixed) detectors for continuous and simultaneous SAXS and wide-angle X-ray scattering (WAXS) acquisition up to 2θ = 60°. The beam path was windowless beam path, entirely under vacuum from beam delivery system to detector sensor. The SAXS patterns were obtained over a scattering vector length within the range of 0.008 $Å^{-1}$ < q < 0.18 $Å^{-1}$. 1D fitting of the scattering curves was obtained by an azimuthal binning and averaging of corresponding 2D scattering patterns using the XSACT (X-Ray Scattering Analysis and Calculation Tool) supplied with the instruments. N_2 physisorption analysis was performed at −196 °C using a Quantachrome Quadrasorb Evo. Before N_2 adsorption measurements, samples were degassed at 300 °C for 6 h. Isotherms were directly measured from the instrument. Total specific surface areas (Sa) were calculated from isotherms based on the Brunauer–Emmett–Teller (BET) theory. Pore size analysis was obtained from the obtained isotherms using the DFT method. X-ray absorption near edge spectroscopy (XANES) was performed using an EasyXAFS 300+ lab-based X-ray absorption spectrometer, fitted with an Ag Lα anode, and an Si 400 spherically bent crystal analyzer. Data was calibrated to a Ti metal foil standard (Goodfellows, 0.005 mm light tight foil) and analyzed using Athena, Demeter suite 0.9.27.

Soft energy XANES (NEXAFS – Near edge X-ray absorption fine structure) data was collected at beamline VerSoX (B07) at Diamond Light Source, UK (photon energy range: 45–2200 eV). A 600 lines mm^{-1} plane grating monochromator with a CFF of 2.25 mm was used. Ti L-edge (450–500 eV, 0.01 eV step), O K-edge (520–560 eV, 0.05 eV step), and Si K-edge (820–850 eV, 0.1 eV step) measurements were performed.

NH_3-TPD profiles were recorded on a ChemBET from Quantachrome instruments equipped with a thermal conductivity detector (TCD). For each experiment, 0.100 g of sample was supported by quartz wool in a U-bend quartz tube. Samples were pre-treated in pure helium, heated at 10 °C min^{-1} to 400 °C for 1 h, and then cooled to 60 °C. A mixture of 5% ammonia in helium were passed over the sample at a rate of 30 mL min^{-1} for 60 min, and then physisorbed ammonia was removed by flushing with 30 mL min^{-1} of pure helium for 1 h whilst holding at 60 °C. The temperature was then increased by 10 °C min^{-1} to 800 °C and gas effluent monitored in this period for ammonia removal.

Photocatalyzed Furfural Aldol Cross-Condensation: Batch aldol cross-condensation reactions performed using a Uniqsis Illumin8 photoreactor (10 W, 365 nm) at atmospheric pressure. In a typical experiment, 30 mmol cyclopentanone, 10 mmol furfural, and 0.1 mmol *n*-dodecane (internal standard) added to a sealed reactor, containing 0.05 g catalyst, at 80 °C, stirring at 800 rpm. Aliquots withdrawn periodically from the reaction mixture and analyzed by off-line GC after dilution with ethyl acetate using a Shimadzu GC-2010 Plus FID system and BP50 30 m × 0.32 mm × 0.25 µm capillary column. Control experiments demonstrated negligible substrate conversion (<4%) in the absence of support or catalyst. Additional reactions conducted in the absence of photoirradiation evidence the promotive influence of photoirradiation on catalyst performance and product yield. To ensure consistent optical and dispersion behavior, all Ti-SBA-15 photocatalysts were sieved through a −325 mesh sieve (≈≤44 µm) and sonicated prior to use. Reactions were conducted under continuous stirring to prevent sedimentation and ensure uniform light exposure. This protocol aligns with the previous approach for controlling particle size-dependent reactivity.[45] A reaction temperature of 80 °C was selected as a benchmark to enable direct comparison with literature reported acid-catalyzed furfural upgrading processes, where humin formation becomes significant above this threshold.[46] This temperature minimizes the potential for humin by-product formation and allows evaluation of the promotive effect of photocatalysis over purely thermal pathways, particularly for Lewis acidic Ti-SBA-15 catalysts. Quoted activity and selectivity values are the mean of triplicate reactions with errors ±3%; mass balances >93% in all cases. Furfural conversion was calculated from Equation 1, where n_t is the mmol furfural at time t, and n_0 the initial mmol furfural, and selectivity calculated from Equation 2 based exclusively on the observed liquid phase products, where $n_{x=i}$ is the mmol of product, i and Σn_x denotes the total mmol of all products. Product yield calculated from Equation 3. Mass-normalized initial rates calculated from the first hour of reaction. Reaction products, FCp-OH, FCp and F_2Cp, were synthesized and purified via literature methods[47] for quantification in catalytic testing, as they are not commercially available, further verified using an Agilent 7890A GC system equipped with a 5975C Triple-Axis MS detector and HP-5MS 30 m × 0.25 mm × 0.25 µm column (Figure S21a–c, Supporting Information).

$$\text{Conversion } (\%) = [(n_0 - n_t) / (n_0)] \times 100 \quad (1)$$

$$\text{Selectivity } (\%) = [(n_{x=i}) / (\Sigma n_x)] \times 100 \quad (2)$$

$$\text{Yield } (\%) = (\text{Conversion} \times \text{Selectivity}) / 100 \quad (3)$$

Supporting Information

Supporting Information is available from the Wiley Online Library or from the author.

Acknowledgements

The authors thank the EPSRC (grants EP/Y023587/1, EP/Y023609/1, EP/Y023536/1, EP/Y023552/1 and EP/Y023544/1 – National Facility for XPS ("HarwellXPS")), RSC (R19-2791 and M19-1518), Innovate UK "Flexible, agile, scalable and sustainable medicines Manufacturing" call funding and the University of Plymouth's R&D solutions fund for facilitating this work. The authors would like to thank the UCL MAPS summer internship scheme/Ivan Parkin, The Dean of MAPS at UCL for funding the placements of J.L. and S.K. for this project. The authors would also like to thank Dr. Robert Clough and Louise Argent for their help with ICP-MS and GC analyses, respectively (UoP). The authors would like to thank Gavin Stenning for help with SAXS analysis in the Materials Characterisation Laboratory at the ISIS Neutron and Muon Source. The authors appreciate the award of instrument time at the Diamond Light Source B07 beamline under proposal SI40403-1.

Conflict of Interest

The authors declare no conflict of interest.

Author Contributions

M.A.I. and L.D. performed conceptualization. M.A.I., S.K., C.M.A.P., J.L., A.T. and C.P. performed synthesis of materials. M.A.I., A.G., S.K., J.L., C.P., L.D., A.T., C.M.A.P. and C.D. performed materials characterization. M.A.I., S.K., J.L., C.P. and L.D. performed data analysis. L.D. and V.S.D. performed catalytic testing. M.A.I. and L.D. wrote the original manuscript.

Data Availability Statement

The data that support the findings of this study are available from the corresponding author upon reasonable request.

Keywords

hierarchical titania, photocatalysis, sustainable aviation fuels

Received: January 29, 2025
Revised: May 29, 2025
Published online:

[1] H. Ritchie, What share of global CO_2 emissions come from aviation? 2024, https://ourworldindata.org/global-aviation-emissions#article-citation (accessed: November 2024).
[2] M. Klöwer, M. R. Allen, D. S. Lee, S. R. Proud, L. Gallagher, A. Skowron, *Environ. Res. Lett.* **2021**, *16*, 104027.
[3] A. Rödl, *Biokerosene: status and prospects* **2018**, *9*, 189.
[4] R. Ahorsu, F. Medina, M. Constantí, *Energies* **2018**, *11*, 3366.
[5] S. S. Doliente, A. Narayan, J. F. D. Tapia, N. J. Samsatli, Y. Zhao, S. Samsatli, *Front. Energy Res.* **2020**, *8*, 110.
[6] M. Millinger, J. Ponitka, O. Arendt, D. Thrän, *Energy Policy* **2017**, *107*, 394.
[7] a) A. F. Lee, K. Wilson, *Catal. Today* **2015**, *242*, 3; b) A. C. Lamb, A. F. Lee, K. Wilson, *Aust. J. Chem.* **2020**, *73*, 832; c) M. Sankar, N. Dimitratos, P. J. Miedziak, P. P. Wells, C. J. Kiely, G. J. Hutchings, *Chem. Soc. Rev.* **2012**, *41*, 8099; d) S. Ding, C. M. Parlett, X. Fan, *Mol. Catal.* **2022**, *523*, 111492.
[8] a) S. Kang, J. Fu, G. Zhang, *Renew. Susta. Energy Rev.* **2018**, *94*, 340; b) P. Khemthong, C. Yimsukanan, T. Narkkun, A. Srifa, T. Witoon, S. Pongchaiphol, S. Kiatphuengporn, K. Faungnawakij, *Biomass Bioenergy* **2021**, *148*, 106033.
[9] a) M. J. Climent, A. Corma, S. Iborra, *Green Chem.* **2014**, *16*, 516; b) Y. Nakagawa, M. Tamura, K. Tomishige, *Fuel Process. Technol.* **2019**, *193*, 404.
[10] a) B. A. Mehrabadi, S. Eskandari, U. Khan, R. D. White, J. R. Regalbuto, *Adv. Catal.* **2017**, *61*, 1; b) L. Wang, J. Wu, S. Wang, H. Liu, Y. Wang, D. Wang, *Nano Res.* **2023**, *17*, 3261; c) C. M. Parlett, K. Wilson, A. F. Lee, *Chem. Soc. Rev.* **2013**, *42*, 3876; d) D. Chen, X. Zhang, A. F. Lee, *J. Mater. Chem. A* **2015**, *3*, 14487; e) K. Ralphs, C. Hardacre, S. L. James, *Chem. Soc. Rev.* **2013**, *42*, 7701.
[11] a) L. Smoláková, K. Frolich, J. Kocík, O. Kikhtyanin, L. Čapek, *Ind. Eng. Chem. Res.* **2017**, *56*, 4638; b) X. Zhang, Y. Li, C. Qian, L. An, W. Wang, X. Li, X. Shao, Z. Li, *RSC Adv.* **2023**, *13*, 9466; c) J. He, Q. Qiang, S. Liu, K. Song, X. Zhou, J. Guo, B. Zhang, C. Li, *Fuel* **2021**, *306*, 121765.
[12] a) F. Bérubé, B. Nohair, F. Kleitz, S. Kaliaguine, *Chem. Mater.* **2010**, *22*, 1988; b) X. Zhang, L. J. Durndell, M. A. Isaacs, C. M. Parlett, A. F. Lee, K. Wilson, *ACS Catal.* **2016**, *6*, 7409; c) P. Wu, T. Tatsumi, T. Komatsu, T. Yashima, *Chem. Mater.* **2002**, *14*, 1657.
[13] J. Kijenski, A. Baiker, M. Glinski, P. Dollenmeier, A. Wokaun, *J. Catal.* **1986**, *101*, 1.
[14] a) A. Fernandez, J. Leyrer, R. Agusti'n, G. Munuera, H. Knözinger, *J. Catal.* **1988**, *112*, 489; b) P. Iengo, G. Aprile, M. Di Serio, D. Gazzoli, E. Santacesaria, *Appl. Catal., A* **1999**, *178*, 97.
[15] a) M. A. Isaacs, C. M. Parlett, N. Robinson, L. J. Durndell, J. C. Manayil, S. K. Beaumont, S. Jiang, N. S. Hondow, A. C. Lamb, D. Jampaiah, *Nat. Catal.* **2020**, *3*, 921; b) C. M. Parlett, M. A. Isaacs, S. K. Beaumont, L. M. Bingham, N. S. Hondow, K. Wilson, A. F. Lee, *Nat. Mater.* **2016**, *15*, 178.
[16] J. A. Mejías, V. M. Jiménez, G. Lassaletta, A. Fernández, J. P. Espinós, *J. Phys. Chem.* **1996**, *100*, 16255.
[17] X. Gao, S. R. Bare, J. L. G. Fierro, M. A. Banares, I. E. Wachs, *J. Phys. Chem. B* **1998**, *102*, 5653.
[18] J. Debgupta, L. Lari, M. Isaacs, J. Carey, K. P. McKenna, V. K. Lazarov, V. Chechik, R. E. Douthwaite, *J. Phys. Chem. C* **2023**, *127*, 660.
[19] J. T. Miller, M. Schreier, A. J. Kropf, J. R. Regalbuto, *J. Catal.* **2004**, *225*, 203.
[20] W. Wang, X. Ji, H. Ge, Z. Li, G. Tian, X. Shao, Q. Zhang, *RSC Adv.* **2017**, *7*, 16901.
[21] D. N. Thanh, O. Kikhtyanin, R. Ramos, M. Kothari, P. Ulbrich, T. Munshi, D. Kubička, *Catal. Today* **2016**, *277*, 97.
[22] I. Agirrezabal-Telleria, J. Requies, M. B. Güemez, P. L. Arias, *Appl. Catal., B* **2012**, *115–116*, 169.
[23] a) HIGFLY, Jet fuel production from biobased molecules via catalytic condensation 2024, https://www.higfly.eu/news/jet-fuel-production-biobased-molecules-catalytic-condensation (accessed: November **2024**). b) H. Olcay, A. V. Subrahmanyam, R. Xing, J. Lajoie, J. A. Dumesic, G. W. Huber, *Energy Environ. Sci.* **2013**, *6*, 205; c) R. Baldenhofer, A. Smet, J. P. Lange, S. R. A. Kersten, M. P. Ruiz, *Biomass Bioenergy* **2024**, *190*, 107410.
[24] S. Mamedov, *Spec. Supplements* **2020**, *35*, 41.
[25] G. C. Smith, *J. Electron Spectrosc. Relat. Phenom.* **2005**, *148*, 21.
[26] a) S. Tanuma, C. Powell, Penn, D. R., *Surf. Interface Anal* **1994**, *21*, 165; b) S. M. Tougaard, QUASES-Inelastic electron mean free path calculator (by TPP2M formula), Zenodo, **2021**.
[27] a) M. A. Isaacs, B. Barbero, L. J. Durndell, A. C. Hilton, L. Olivi, C. M. Parlett, K. Wilson, A. F. Lee, *Antibiotics* **2018**, *7*, 55; b) C. M. Parlett, L. J. Durndell, A. Machado, G. Cibin, D. W. Bruce, N. S. Hondow, K. Wilson, A. F. Lee, *Catal. Today* **2014**, *229*, 46.
[28] P. Bhatt, M. Isaacs, Y. Liu, R. G. Palgrave, *Appl. Surf. Sci.* **2024**, *672*, 160808.
[29] G. Moretti, *Surf. Interface Anal.* **1990**, *16*, 159.
[30] M. C. Biesinger, L. W. Lau, A. R. Gerson, R. S. C. Smart, *Phys. Chem. Chem. Phys.* **2012**, *14*, 2434.
[31] P. Ascarelli, G. Moretti, *Surf. Interface Anal.* **1985**, *7*, 8.
[32] J. Zhang, Z. Ma, J. Jiao, H. Yin, W. Yan, E. W. Hagaman, J. Yu, S. Dai, *Langmuir* **2009**, *25*, 12541.
[33] M. A. Isaacs, P. R. Davies, A. Graf, D. J. Morgan, R. Palgrave, *Surf. Interface Anal.* **2025**, *57*, 548.
[34] S. Kucheyev, T. Van Buuren, T. Baumann, J. Satcher Jr, T. Willey, R. Meulenberg, T. Felter, J. Poco, S. Gammon, L. Terminello, *Phys. Rev. B* **2004**, *69*, 245102.
[35] M. Vos, S. W. King, B. L. French, *J. Electron Spectrosc. Relat. Phenom.* **2016**, *212*, 74.
[36] N. C. Diamantopoulos, A. Barnasas, C. S. Garoufalis, D. I. Anyfantis, N. Bouropoulos, P. Poulopoulos, S. Baskoutas, *Nanomaterials* **2020**, *10*, 2379.
[37] B. Boekaerts, W. Lorenz, J. Van Aelst, B. F. Sels, *Appl. Catal., B* **2022**, *305*, 121052.
[38] M. Xu, Y. Gao, E. M. Moreno, M. Kunst, M. Muhler, Y. Wang, H. Idriss, C. Wöll, *Phys. Rev. Lett.* **2011**, *106*, 138302.
[39] a) W. Lin, Y. Zhang, Z. Ma, Z. Sun, X. Liu, C. C. Xu, R. Nie, *Appl. Catal., B* **2024**, *340*, 123191; b) S. Borghei, S. Hosseini, *Chem. Eng. J.* **2008**, *139*, 482; c) S. Lv, H. Liu, J. Zhang, Q. Wu, F. Wang, *J. Energy Chem.* **2022**, *73*, 259.

[40] a) J. Cueto, D. de la Calle, M. d. Mar Alonso-Doncel, E. A. Giner, R. A. García-Muñoz, D. P. Serrano, *Bioresour. Technol.* **2025**, *418*, 131877; b) P. Kostestkyy, J. Yu, R. J. Gorte, G. Mpourmpakis, *Catal. Sci. Technol.* **2014**, *4*, 3861.

[41] D. Yang, H. Liu, Z. Zheng, Y. Yuan, J.-c. Zhao, E. R. Waclawik, X. Ke, H. Zhu, *J. Am. Chem. Soc.* **2009**, *131*, 17885.

[42] a) X. Bao, H. Li, Z. Wang, F. Tong, M. Liu, Z. Zheng, P. Wang, H. Cheng, Y. Liu, Y. Dai, *Appl. Catal., B* **2021**, *286*, 119885; b) S. Higashimoto, N. Kitao, N. Yoshida, T. Sakura, M. Azuma, H. Ohue, Y. Sakata, *J. Catal.* **2009**, *266*, 279.

[43] M. Landau, E. Dafa, M. Kaliya, T. Sen, M. Herskowitz, *Microporous Mesoporous Mater.* **2001**, *49*, 65.

[44] C. Maheu, L. Cardenas, E. Puzenat, P. Afanasiev, C. Geantet, *Phys. Chem. Chem. Phys.* **2018**, *20*, 25629.

[45] L. J. Durndell, C. M. Parlett, N. S. Hondow, M. A. Isaacs, K. Wilson, A. F. Lee, *Sci. Rep.* **2015**, *5*, 9425.

[46] a) Q. Liu, X. Zhang, Q. Zhang, Q. Liu, C. Wang, L. Ma, *Energy Fuels* **2020**, *34*, 7149; b) W. Wang, X. Ji, H. Ge, Z. Li, G. Tian, X. Shao, Q. Zhang, *RSC Adv.* **2017**, *7*, 16901; c) O. Kikhtyanin, V. Kelbichová, D. Vitvarová, M. Kubů, D. Kubička, *Catal. Today* **2014**, *227*, 154; d) E. D. Saluta, M. N. Gebresillase, J. G. Seo, *Adv. Energy Susta. Res.* **2025**, *6*, 2400369.

[47] M. a. d. M. Alonso-Doncel, E. A. Giner, D. de la Calle, J. Cueto, P. Horcajada, R. A. García-Muñoz, D. P. Serrano, *Cryst. Growth Des.* **2023**, *23*, 5658.